ACS APPLIED MATERIALS & INTERFACES

Research Article

www.acsami.org

In Vitro and *in Vivo* Studies of Novel Poly(D,L-lactic acid), Superhydrophilic Carbon Nanotubes, and Nanohydroxyapatite Scaffolds for Bone Regeneration

Idalia A. W. B. Siqueira,[†,#] Marcus Alexandre F. Corat,[‡] Bruno das Neves Cavalcanti,[§] Wilson Alves Ribeiro Neto,[∥] Airton Abrahao Martin,[⊥] Rosario Elida Suman Bretas,[∥] Fernanda Roberta Marciano,[†] and Anderson Oliveira Lobo*[,†,#]

[†]Laboratory of Biomedical Nanotechnology (NANOBIO), Institute of Research and Development (IP&D II), University of Vale do Paraiba (UNIVAP), Sao Jose dos Campos SP 12244-000, Sao Paulo, Brazil

[‡]Multidisciplinary Center for Biological Investigation on Laboratory Animal Science (CEMIB), State University of Campinas, Campinas SP 13083-970, Sao Paulo, Brazil

[§]Department of Cariology, Restorative Sciences and Endodontics, School of Dentistry, University of Michigan, Ann Arbor, Michigan 48109, United States

[∥]Department of Materials Engineering, Federal University of Sao Carlos, Sao Carlos SP 13565-905, Sao Paulo, Brazil

[⊥]Laboratory of Biomedical Vibrational Spectroscopy, Institute of Research and Development (IP&D II), University of Vale do Paraiba (UNIVAP), Sao Jose dos Campos SP 12244-000, Sao Paulo, Brazil

ABSTRACT: Poly(D,L-lactide acid, PDLLA) has been researched for scaffolds in bone regeneration. However, its hydrophobocity and smooth surface impedes its interaction with biological fluid and cell adhesion. To alter the surface characteristics, different surface modification techniques have been developed to facilitate biological application. The present study compared two different routes to produce PDLLA/superhydrophilic vertically aligned carbon nanotubes:nanohydroxyapatite (PDLLA/VACNT-O:nHAp) scaffolds. For this, we used electrodeposition and immersion in simulated body fluid (SBF). Characterization by goniometry, scanning electron microscopy, X-ray diffraction, and infrared spectroscopy confirmed the polymer modifications, the *in vitro* bioactivity, and biomineralization. Differential scanning calorimetry and thermal gravimetric analyses showed that the inclusion of VACNT-O:nHA probably acts as a nucleating agent increasing the crystallization rate in the neat PDLLA without structural alteration. Our results showed the formation of a dense nHAp layer on all scaffolds after 14 days of immersion in SBF solution; the most intense carbonated nHAp peaks observed in the PDLLA/VACNT-O:nHAp samples suggest higher calcium precipitation compared to the PDLLA control. Both cell viability and alkaline phosphatase assays showed favorable results, because no cytotoxic effects were present and all produced scaffolds were able to induce detectable mineralization. Bone defects were used to evaluate the bone regeneration; the confocal Raman and histological results confirmed high potential for bone applications. *In vivo* study showed that the PDLLA/VACNT-O:nHAp scaffolds mimicked the immature bone and induced bone remodeling. These findings indicate surface improvement and the applicability of this new nanobiomaterial for bone regenerative medicine.

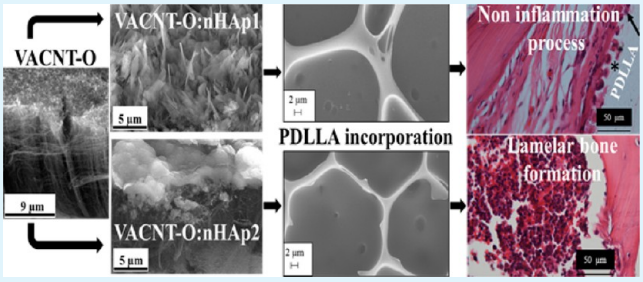

KEYWORDS: *carbon nanotube, PDLLA, nanohydroxyapatite, bone regeneration, porous scaffold, bioactivity*

1. INTRODUCTION

New perspectives show that bioresorbable polymers can be successful bone substitutes. This is due to biocompatibility, reabsorption with gradual transfer of load, and promotion of bone stimulation and, also, due to a nonsurgical intervention to remove material.[1−3] Poly(D,L-lactide acid) (PDLLA) is a biocompatible and biodegradable polymer, with a fast and controllable degradation time.[3] However, this polymer presents hydrophobic character, which allows primary interactions with the aqueous biosystem.[4,5] Furthermore, PDLLA has low mechanical resistance, limiting its application for regenerative bone medicine.[6] Therefore, the development of polymer nanocomposites with a mixture of polymer matrix and nanoscale fillers can improve cell interaction and mechanical properties.

The physiological response to biomaterials depends on the materials' topography characteristics, as well as the implant location and interaction with the biological systems. During the

Received: September 8, 2014
Accepted: April 22, 2015
Published: April 22, 2015

DOI: 10.1021/acsami.5b01066
ACS Appl. Mater. Interfaces 2015, 7, 9385−9398

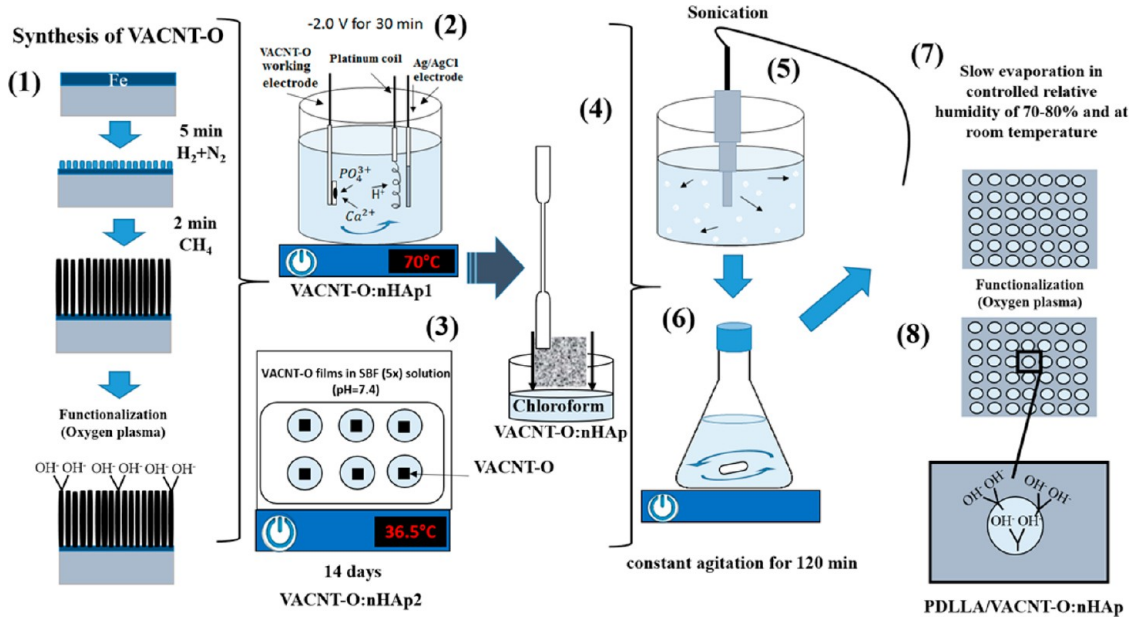

Figure 1. Scheme of scaffolds production.

osseointegration, connective tissue can be formed on the material surface, and this tissue can compromise bone formation, in which case an osteoinductive bioimplant is necessary.[7,8]

Aiming to support the osseointegration, several studies have investigated the means to improve the polymer characteristics, such as the incorporation of osteoinductive nanoparticles and surface treatments. The incorporation of carbon nanotubes (CNTs) and hydroxyapatite (HAp) into the polymer matrix is an alternative to improve the physical, chemical, and biological polymer characteristics as well as to formulate a material that mimics bone tissue.[9−11]

To date, our group has developed biomimetic nanoparticles and evaluated the behavior using cell culture.[12,13] For instance, superhydrophilic vertically aligned CNTs (VACNT-O) are promising for biomedical applications due to their properties of mechanical strength, high chemical stability, and functionalization.[12,13] In a recent study, the production of nanofibers with dispersed CNTs into poly(lactic acid) (PLLA) matrix resulted in an electrical conductor scaffold that improved the osteoblast functions.[11] In addition, osteoinductive nanoparticles such as nanohydroxyapatite (nHAp) can be deposited on CNTs by low-cost methods, such as electrodeposition and immersion in simulated body fluid (SBF) solution,[13,14] to improve the mechanical and bioactivity properties. Contributing to this, our group developed a fast and homogeneous method to produce nHAp:VACNT-O scaffolds,[13] with interesting biomineralization properties, human osteoblast adhesion, and lamellar bone formation.[13−15]

The VACNT-O biomineralization process[16] resulted from apatite nanocrystals precipitation on the VACNT surface after immersion in 5 × SBF[17,18] solutions up to 7 days. Data show the formation of an nHAp dense layer with a globular morphology similar to biological nHAp as well as cell adhesion and proliferation.[16] Based on these results, we demonstrated that nHap obtained by electrodeposition and soaked in SBF solution is biocompatible, improves the osteoblast cell attachment, is bioactive, and promotes *in vivo* bone regeneration.[15]

Here we present two new methodologies to obtain porous and rough hydrophilic PDLLA scaffolds with incorporated VACNT-O:nHAp nanoparticles into the polymer matrix. For these, we used the honeycomb method to control the humidity condition. Briefly, these new proposed methodologies consist of the following: (i) nHAp crystals directly electrodeposited onto VACNT-O (nHAp1) and then dispersed in PDLLA solution at controlled humidity[19] or (ii) VACNT-O soaked in SBF solution to produce nHAp crystals (nHAp2) and then dispersed in PDLLA solution at controlled humidity to produce honeycomb scaffolds. After this, we functionalize these new nano-biomaterials using oxygen plasma treatment to obtain hydrophilic properties. We associated these properties with *in vitro* bioactivity, biomineralization process, cell spreading, adhesion, and *in vivo* assay. Therefore, we developed porous hydrophilic PDLLA/VACNT-O:nHAp scaffolds for osteoregeneration.

2. METHODOLOGY

2.1. Production of VACNT-O:nHAp Nanoparticles to Polymer Matrix Dispersion. *2.1.1. Synthesis of VACNT-O.* We produced VACNT-O as a thin film, using a microwave plasma chamber at 2.45 GHz (MWCVD) as shown elsewhere.[20] Briefly, the substrates were 10 mm titanium (Ti) squares, covered by a thin Fe layer (10 nm). The Fe layers were pretreated to promote nanocluster formation, which forms the catalyst for VACNT growth. The pretreatment was carried out for 5 min in N_2/H_2 (10/90 (cm^3(STP) min^{-1})) plasma, at a substrate temperature around 760 °C. After pretreatment, CH_4 (14 cm^3(STP) min^{-1}) was inserted into the chamber at a substrate temperature of 800 °C for 2 min. The reactor was kept at a pressure of 30 Torr during the whole process. Functionalization of the VACNT tips by incorporating oxygen-containing groups was performed in a pulsed direct current plasma reactor with an oxygen flow rate of 1 cm^3(STP) min^{-1}, at a pressure of 85 mTorr, 700 V, and with a frequency of 20 kHz (called VACNT-O). The total time of the plasma etching was 120 s.[20]

2.1.2. Electrodeposition of nHAp Crystals on VACNT-O (nHAp1). The electrodeposition of the nHAp crystals on VACNT-O films was performed using 0.042 mol·L^{-1} calcium nitrate tetrahydrate ($Ca(NO_3)_2{\cdot}4H_2O$) and 0.025 mol·L^{-1} ammonium hydrogen phosphate ($(NH_4){\cdot}2HPO_4$) electrolyte solutions (pH = 4.8). These concen-

DOI: 10.1021/acsami.5b01066
ACS Appl. Mater. Interfaces 2015, 7, 9385−9398

trations were chosen so that Ca/P = 1.67. We used classical electrochemical equipment. Briefly, we used a three-electrode cell coupled to Autolab PGSTAT 128N equipment. VACNT-O films were used as the working electrode, and the geometric area in contact with electrolytic solution was 0.27 cm^2. A platinum coil wire served as auxiliary electrode, and an Ag/AgCl electrode was used as reference electrode. The nHAp crystals were produced by applying a constant potential of −2.0 V for 30 min, and the solution temperature was maintained at 70 °C in magnetic stirrer.[13]

2.1.3. Production of VACNT-O:nHAp Scaffolds by Biomimetic Simulated Body Fluid Method (nHAp2). We soaked VACNT-O films in SBF (5×) solution (pH = 7.4) to produce nHAp crystals, with the following components and concentrations in SBF (5×) solution: NaCl, 733.5 mM; $MgCl_2{\cdot}6H_2O$, 7.5 mM; $CaCl_2{\cdot}2H_2O$, 12.5 mM; $Na_2HPO_4{\cdot}2H_2O$, 5.0 mM; $NaHCO_3$, 21.0 mM.[17,18]

VACNT-O samples were placed in polyethylene tubes and exposed to UV light in the biosafety chamber (BioProtector-12 Plus VECO) for 30 min. Next, 13 mL of SBF solution was added to the membranes, and then the samples were stored in a refrigerated incubator (Cientec, CT-712-R) in constant agitation at 75 rpm in 36.5 °C for 14 days. After the incubation, the samples were washed in deionized water and dried in an incubator (SP400, SPLABOR) at 50 °C for 1 h.[16]

2.1.4. Production of Porous PDLLA/VACNT-O:nHAp Scaffolds. We removed all of the nanoparticles (nHAp1 and nHAp2) from their respective Ti subtracts and transferred them to chloroform solution (0.3% w/v). Next, we separately dispersed the nHAp1 and nHAp2 nanoparticles under ultrasound irradiation for 2 min (SONIC-VCX500, 1200 J mL^{-1}) in 20 mL of chloroform. We kept the temperature less than 40 °C.[21] After this, we diluted PDLLA (Purasorb PLD-9655, 162 copolymer of L-lactide; Puracbiochem, Gorinchem, Holland) in chloroform solution (5% w/v) content nHAp1 and nHAp2 dispersed nanoparticles under magnetic stirrer for 120 min. We inserted the solutions into a square mold with 0.5 mm diameter and dried them in ambient temperature for 12 h under slow evaporation at controlled relative humidity of 70−80% and at room temperature. We performed a simple and fast functionalization to obtain hydrophilic character due to incorporation of oxygen-containing groups, using a pulsed-DC plasma reactor with an oxygen flow rate of 1 cm^3(STP) min^{-1}, at a pressure of 85 mTorr, 700 V, at a repetition rate of 20 kHz.[20] We used PDLLA membranes without any incorporated nanoparticles or oxygen plasma treatment as controls.

2.1.5. Scheme of Scaffolds Production. Figure 1 shows a scheme of the scaffold production. Number 1 describes the VACNT production and functionalization (VACNT-O). Number 2 describes the electrodeposition of nHAp crystals on VACNT-O (nHAp1). Number 3 shows the production of VACNT-O:nHAp scaffolds by biomimetic simulated body fluid method (nHAp2). After that, all of the nanoparticles (nHAp1 and nHAp2) were removed from their respective Ti subtracts and transferred to a chloroform solution (4). Number 5 shows the dispersion of the nHAp1 and nHAp2 nanoparticles under ultrasound irradiation in chloroform; the polymer solution was homogenized under constant agitation for 120 min (6). Number 7 shows the pouring of the polymer solution into a square mold with 0.5 mm diameter and subsequent drying at ambient temperature for 12 h with slow evaporation in controlled relative humidity of 70−80% and at room temperature. Number 8 shows the oxygen plasma treatment to the incorporation of oxygen-containing groups.

2.2. *In Vitro* Bioactivity Assay. We evaluated the carbonated nHAp precipitation on PDLLA/VACNT-O:nHAp scaffolds soaking in SBF (5×) solution (pH = 7.4) up to 14 days. For preparing the SBF (5×) solution, we used the following: NaCl, 733.5 mM; $MgCl_2{\cdot}6H_2O$, 7.5 mM; $CaCl_2{\cdot}2H_2O$, 12.5 mM; $Na_2HPO_4{\cdot}2H_2O$, 5.0 mM; $NaHCO_3$, 21.0 mM.[16,17] PDLLA/VACNT-O:nHAp scaffolds were placed in polyethylene tubes and exposed to UV light in the biosafety chamber (BioProtector-12 Plus VECO) for 30 min. After this, we added 13 mL of SBF solution into the tube and stored it in a refrigerated incubator (Cientec, CT-712-R) in constant agitation at 75 rpm and at 36.5 °C for 14 days. After the incubation time, we washed the samples using deionized water and then dried them in an incubator (SP400, SPLABOR) at 50 °C for 1 h.[16]

2.3. Scaffolds Characterization. *2.3.1. PDLLA/VACNT-O:nHAp Characterization.* We collected micrographs using high resolution scanning and transmission electron microscopy (HR-SEM (FEI Inspect F50) and HR-TEM (FEI TECNAI G^2 F20 and Philips CM-120)) to characterize the morphological and structural properties of samples. Also, we used an optical profilometer (WYKO NT 1100 series optical profiling system) for topography and roughness measurements.

We performed the porosity analyses using the immersion method. For this, we immersed the bioscaffolds into *n*-butanol for 2 h. Next, we dried the scaffolds using filter paper.[22] We calculated the porosity using eq 1:[22]

$$\in = \frac{m_b/\rho_b}{\frac{m_b}{\rho_b} + \frac{m_p}{\rho_p}} \quad (1)$$

where ∈ is the porosity, m_b is the mass absorbed of *n*-butanol, m_p is the mass of the membrane, ρ_b is the density of *n*-butanol, and ρ_p is the density of PDLLA.

The thermal behavior of 5 mg of each sample was studied by differential scanning calorimetry (DSC; TA Instruments, model Q100). The heating was done from 25 to 200 °C, at 10 °C min^{-1}, for all samples. From the heat of melting, the amount of crystallinity (% C) was calculated using the following eq 2:

$$\%\, C = \frac{\Delta H_m - \Delta H_{cc}}{\Delta H_0} \quad (2)$$

where ΔH_{cc} is the cold crystallization enthalpy (when present), ΔH_m is the melting enthalpy of the sample, and ΔH_0 is the melting enthalpy of a 100% crystalline sample. For the PDLLA, ΔH_0 = 93 J g^{-1}.[23]

The amount of residual solvent (when present) was calculated with eq 3:

$$\Delta H_v = m(c\Delta T + L) \quad (3)$$

where ΔH_v is the vaporization endotherm, m is the mass of the vaporized residual solvent (kg), c is the specific heat capacity of the solvent, Δ_T = (end vaporization temperature − initial vaporization temperature), and L is the latent heat of vaporization of the solvent. The percentage of residual solvent (% RS) was calculated from eq 4:[23]

$$\%\,\mathrm{RS} = \frac{m}{m_T} \times 100 \quad (4)$$

where m_T = DSC sample mass (kg).

Thermogravimetric analyses (TGA) were performed using a thermal analyzer (TA Instruments, model TGA Q500). We used a heating rate of 10 °C/min and using nitrogen as the inert atmosphere. We analyzed a range between 20.0 and 800.0 °C. Measurements were taken using a sample mass of ±0.5 mg for all produced scaffolds.

We used the attenuated total reflection Fourier transform infrared (ATR-FTIR) spectra for collecting superficial functional groups before and after oxygen plasma treatment. We collected this in point mode by transmission at the 700−4000 cm^{-1} interval, the numbers of scans performed, and a resolution of cm^{-1} using a Spectrum Spotlight 400 FT-IR (PerkinElmer) spectrophotometer equipped with MCT detector operating in refrigeration by liquid nitrogen.

We performed the contact angle (CA) measurements using an Easy Drop contact angle measuring instrument model (Kruss Easy Drop DSA 100S) by the sessile drop technique with deionized water (2 μL) and diiodomethane (2 μL) in temperature and pressure controlled atmosphere. We performed measurements immediately after the drop deposition on the surface to avoid disturbances by evaporation or adsorption. After this, we calculated the surface energy of each sample group, by the methodology proposed by Owens and Wendt.[24] This surface energy is described as the sum of dispersive (d; associated with nonpolar groups present) and polar (p; associated with polar groups present on the surface) components. The hydrophobic or hydrophilic character can influence the cell adhesion on the biomaterial.

DOI: 10.1021/acsami.5b01066
ACS Appl. Mater. Interfaces 2015, 7, 9385−9398

We performed the statistical analysis using Graphpad Prisma to compare the scaffold groups for roughness, porous count, and hydrophilic analyses. We applied the t test, and expressed the data as the average of three scaffolds.

The surface energy composed of polar and dispersive components of the samples was evaluated by measuring CA. The interfacial tension between two condensed phases can be determined by Young's equation, according to (eq 5)

$$\cos\theta\gamma_{LV} = \gamma_{SV} - \gamma_{SL} \quad (5)$$

where θ is the measured the CA between liquid and solid, and γ_{LV}, γ_{SV}, and γ_{SL} are the interfacial energies of the liquid/vapor, solid/vapor, and solid/liquid interfaces, respectively. This equation can be rewritten as the Young–Duprè equation (eq 6):

$$W_a = \gamma_{LV}(1 + \cos\theta) = \gamma_{SV} - \gamma_{SL} \quad (6)$$

where W_a is the adhesion energy per unit area of the solid and liquid surfaces. In the general form of eqs 5 and 6, then eq 7 can be written as

$$\gamma_{LV}(1 + \cos\theta) = 2\sqrt{\gamma_L^P\gamma_S^P} + 2\sqrt{\gamma_L^D\gamma_S^D} \quad (7)$$

where γ_L^P and γ_S^P are the polar components of the surface energy of liquid and solid phases, respectively, while γ_L^D and γ_S^D are the dispersive components of the surface energy of the liquid and solid phases, respectively. Because γ_L^D and γ_L^P have been published for many liquids, it is possible to approximate γ_S^D and γ_S^P from a single measurement of θ by the use of eq 7.

Thermodynamically, the bacterial and cell adhesion on a solid surface can be described through the balance of interfacial free energy by the following eq 8.[25]

$$\Delta F_{adh} = \gamma_{SC} - \gamma_{SL} - \gamma_{CL} \quad (8)$$

where ΔF_{adh} is the interfacial free energy of adhesion, γ_{SC} is the solid–cell interfacial free energy, γ_{SL} is the solid–liquid interfacial free energy, and γ_{CL} is the cell–liquid interfacial energy.

The adhesion force is thermodynamically favorable when the result is positive.

The interfacial free energy of adhesion was determined by the following eq 9:[25,26]

$$\Delta F_{adh} = 2(\sqrt{\gamma_S^{LW}\gamma_L^{LW}} + \sqrt{\gamma_S^P\gamma_L^D} + \sqrt{\gamma_S^D\gamma_L^P} + \sqrt{\gamma_C^{LW}\gamma_L^{LW}} + \sqrt{\gamma_C^P\gamma_L^D} + \sqrt{\gamma_C^D\gamma_L^P} - \sqrt{\gamma_S^{LW}\gamma_C^{LW}} - \sqrt{\gamma_S^P\gamma_C^D} - \sqrt{\gamma_S^D\gamma_C^P} - \gamma_L) \quad (9)$$

HR-SEM (model JEOL-JSM 5610 VPI) and HR-TEM (JEOL 3010 at 300 kV with LaB6 filament) were used to characterize the nanoparticles and the scaffolds. We used ImageJ to calculate the porous diameters of the scaffolds.

2.3.2. Bioactivity Characterization. For this, we used two scanning electron microscopes (SEM): (i) model JEOL JSM 5610 VPI was used for the magnifications ranging from 100 to 15,000 times, and (ii) HR-SEM (JSM 6330F) was used for magnifications ranging from 10,000 to 100,000 times.

We used ATR-FTIR spectra to characterize carbonate and phosphate groups formed on scaffolds after biomineralization for 14 days. For these, we obtained, in point mode, transmission and absorption at 700–1000 cm^{-1} interval, the numbers of scans performed, and resolution of cm^{-1} using a Thermo Scientific spectrometer (Nicolet IS model 5) spectrophotometer equipped with 16 scans and a resolution of 4 cm^{-1}.

Analyses of wide-angle X-ray diffractometry were performed using a high resolution Cu Kα radiation generated at 40 kV and 50 mA (Philips X'Pert MRD). All of the results were compared to a standard powder HAp sample (the Joint Committee on Powder Diffraction Standards card 00-019-0272 for carbonate hydroxyapatite).

2.4. Biological *in Vitro* Assays. *2.4.1. Cell Culture.* All experiments were conducted under approval of our Institutional Ethics Board (no. 46420) and were repeated independently 3 times, in order to ensure reproducibility. Normal human osteoblasts were obtained from Lonza (CC-2538, Lonza, Walkersville, MD, USA) and cultured in specific growth media (OGM, CC-3207, Lonza). Cells were used from the third to the fifth passage in all experiments.

2.4.2. Cytotoxicity Assay. Cells were seeded in 24-well plates (1×10^4 cells/well). Control groups were established as follows: a negative control (only cell culture media, no cells) and a positive control (cells cultured in regular culture media). Scaffold groups were established as previously described. Scaffolds were put directly into the medium with no contact with the cells, in order that their degradation products were able to induce cytotoxicity. After 5 days, the scaffolds were removed, cells washed in phosphate buffered saline (PBS, Gibco, Carlsbad, CA, USA), and fixed with 10% trichloroacetic acid (1 h at 4 °C). After washing and drying, cells were stained by a 0.4% sulforodhamine B solution in 1% acetic acid (SRB; Sigma, St. Louis, MO, USA) for 30 min at room temperature. Cells were washed with 1% acetic acid to remove unbound dye and dried. The bound dye was solubilized in 1 mM Tris-base (Sigma) and shaken, and the solution was transferred to a 96-well plate, in order to be read at 570 nm. Data were normalized by the positive cell controls.

2.4.3. Alkaline Phosphatase Assay. Functional mineralization was observed by alkaline phosphatase (ALP) activity. This activity was assessed by using p-nitrophenyl phosphate (pNPP) as the colorimetric substrate (no. 83369, Abcam, Cambridge, U.K.). Control groups were established as described for the cytotoxicity assay, and the effectiveness of the assay was assessed by adding an experimental group with regular media supplemented by dexamethasone and β-glicerophosphate (CC-4194, Lonza), which is well-known for inducing mineralization. After incubation for 5 days, the supernatant was collected and added (50 μL) in triplicate, into a 96-well plate. The substrate was added in each well, and standards were prepared for reading in a microplate reader at 405 nm. Data were tabled as nanomoles of activity per well, according to the values obtained for the standard curve. Negative controls were used to blank the plate. Data were analyzed using software Origin 8.5 by one-way Anova and Tukey ($p < 0.05$).

2.5. *In Vivo* Study. Three groups were used: PDLLA as control, PDLLA/VACNT-O:nHAp1, and PDLLA/VACNT-O:nHAp2. All of the scaffolds were sterilized for 24 h under UV irradiation.

Adult, male, C57BL/6/JUnib mice (22–28 g body weight, (CEMIB/UNICAMP, Campinas, Brazil) were used in this study. All animal procedures were in agreement with the Ethical Principles for Animal Research established by the Brazilian College for Animal Experimentation (COBEA).

This project was approved by the Institutional Ethics Committee for Animal Research at the State University of Campinas (UNICAMP, CEP:3253-1/Brazil). Mice were anesthetized with an intraperitoneal injection with a dose of 225–240 mg kg^{-1} of Avertin (2,2,2-tribromoetanol) using solution at 2.5%. The hair over the calvarium was shaved and cleaned. After the skin was incised, a full thickness circular critically sized defect (diameter of 5 mm) was made in the calvarium using ultrasound equipment CVDent1000 equipped with a sterile CVDENTUS diamond tip under irrigation with sterile normal saline to avoid damage to the bone.

The sterilized minirolls of scaffolds (1 mm diameter and 1 mm of length) matching each group were placed into the defects. The surgical site was irrigated with sterile normal saline, and sterile sutures stitched the wound. In one group of mice, the surgical defect was made and no implant was placed. There were three mice in each group. All mice were followed up daily for signs of infection or discomfort, and they were fed with water and food ad libitum for 4 months. The period of incubation was chosen due to a short degradation time of the PDLLA described in literature.[3] Then the mice were sacrificed by overdose of Halotano (2-bromo-2-chloro-1,1,1-trifluoroethane) inhalation.

2.5.1. Raman Confocal. Block sections of the calvarium containing the disks were harvested from the surgical sites, the bone defect region was sectioned using a diamond blade, and the soft tissues were previously removed.

Confocal Raman measurements were performed on the block sections of the calvarium containing the disks by using a 785 nm laser excitation focused with a 40× lens, 10 s integration time, and 20 mW at the sample. The Raman data were dispersed by a Rivers Diagnosis (Model 3510) and collected by a CCD detector. We analyzed the

DOI: 10.1021/acsami.5b01066
ACS Appl. Mater. Interfaces 2015, 7, 9385–9398

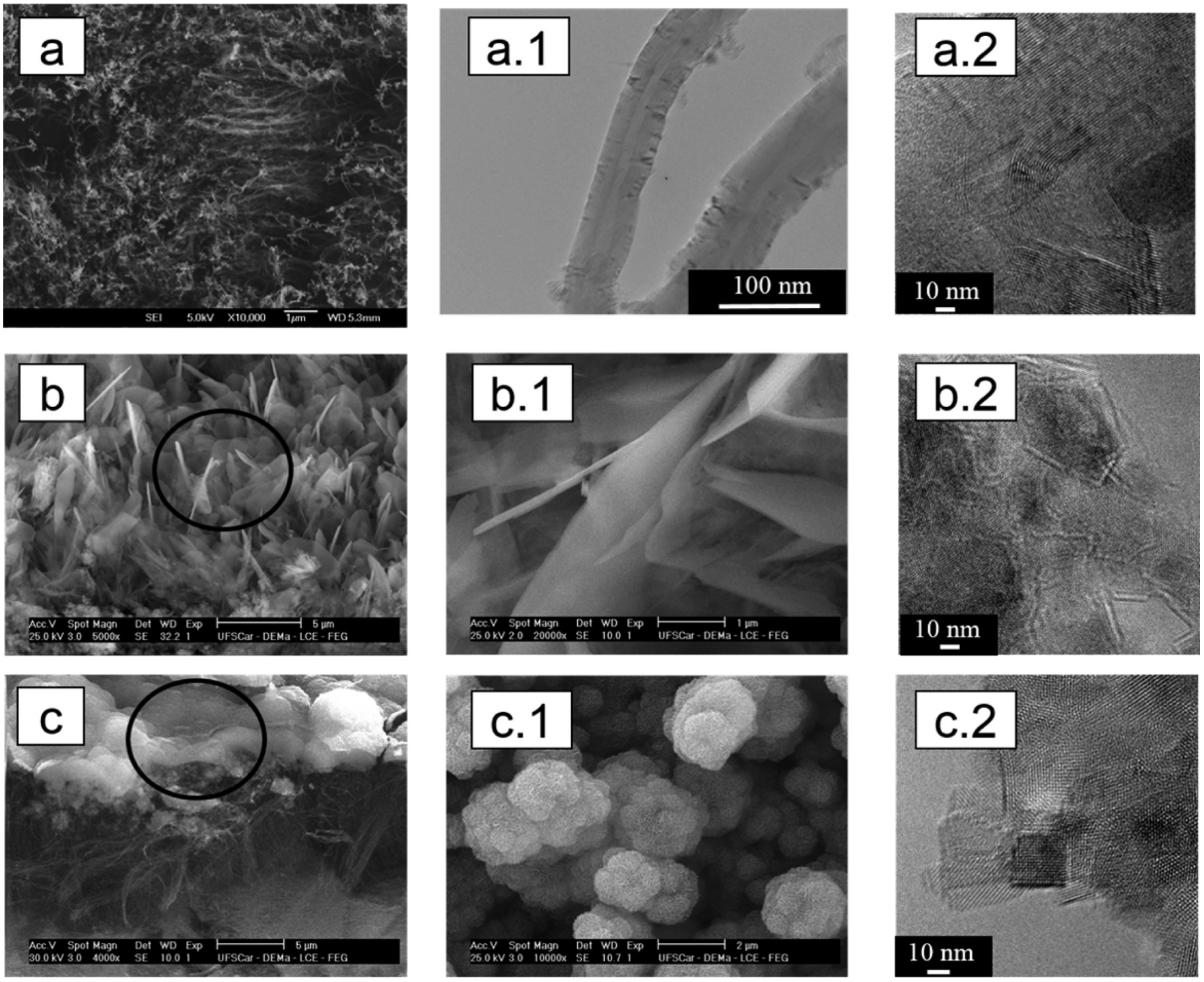

Figure 2. HR-SEM and HR-TEM micrographs: (a) details of VACNT after oxygen plasma exfoliation; (a.1) HR-TEM showing typical bamboo-like structure of VACNT-O; (a.2) HR-TEM showing details of VACNT-O walls; (b) nHAp1 (electrodeposited), details of typical plate-like morphology (b.1 and b.2); (c) nHAp2 (soaked into SBF), details of globular-like morphology (c.1 and c.2). HR-SEM: micrographs a, b, b.1, and c.1. HR-TEM: micrographs a.1, b.2, and c.2.

spectral fingerprint region (400−1800 cm^{-1}) at three different sites from each sample.

2.5.2. Histological Study. Block sections of the calvarium containing the disks were harvested from the surgical sites and fixed in 10% neutral buffered formalin. Specimens were then decalcified in 0.1 M phosphate buffer containing 10% EDTA for 2 weeks and dehydrated for 12 h with a graded series of alcohols. Tissue sections were stained with hematoxylin and eosin (H&E).

2.5.3. SEM Analysis. The specimens were fixed with a 3% glutaraldehyde (0.1 M) sodium cacodylate buffer for 1 h and dehydrated in a graded ethanol solution series (30, 50, 70, 95, and 100%) for 10 min each. The drying stage used a 1:1 solution of ethanol with hexamethyldisilazane (HMDS), and the specimens were dried with pure HMDS at room temperature. After deposition of a thin gold layer, the specimens were examined by SEM.

3. RESULTS AND DISCUSSION

Figure 2 shows HR-SEM and HR-TEM analysis of the as-grown nanoparticles before the dispersion in PDLLA polymeric matrix. Figure 1a shows collected micrographs from as-grown VACNT-O nanoparticles. Figure 2a illustrates details of the exfoliation of the VACNT-O, and parts a.1 and a.2 of Figure 2 show HR-TEM micrographs of typical internal bamboo-like structures of the VACNT-O. Figure 1b shows nHAp2 nanoparticles obtained by the electrodeposition method. Parts b.1 and b.2 of Figure 2 display details of plate-like nHAp obtained by electrodeposition using HR-SEM and HR-TEM, respectively (dimensions ∼ 10−15 nm). Figure 2c shows nHAp1 nanoparticles on VACNT-O obtained after being soaked in SBF solution after 21 days. Parts c.1 and c.2 of Figure 2 illustrate globular nHAp with nanosize diameters observed by HR-SEM and HR-TEM, respectively (dimensions ∼ 10−15 nm). The difference between both nHAp samples is notable. Clearly, the nHAp2 porosity (Figure 2c.1) produced by SBF is higher than that of nHAp1, obtained by electrodeposition.

Figure 3 shows micrographs of the produced PDLLA (Figure 3a), PDLLA/VACNT-O:nHAp1 (Figure 3b), and PDLLA/VACNT-O:nHAp2 (Figure 3c) scaffolds. In general, we observed differences in surface morphology between groups after incorporating the nanoparticles. Figure 2a shows small pores on the surface of PDLLA (∼227 pores counted by ImageJ). After the incorporation of the nHAp1 nanoparticles, the scaffolds had larger pores with diameter between 12 and 31 μm on the surface (∼87 pores counted by imageJ; Figure 3b). However, after the incorporation of the nHAp2 nanoparticles, it presented values between 21 and 35 μm (∼121 pores counted by imageJ; Figure 3c). Thus, increased roughness on PDLLA/VACNT-O:nHAp1 (Figure 3b.1) and PDLLA/VACNT-O:nHAp2 (Figure 3c.1) honeycomb films compared

DOI: 10.1021/acsami.5b01066
ACS Appl. Mater. Interfaces 2015, 7, 9385−9398

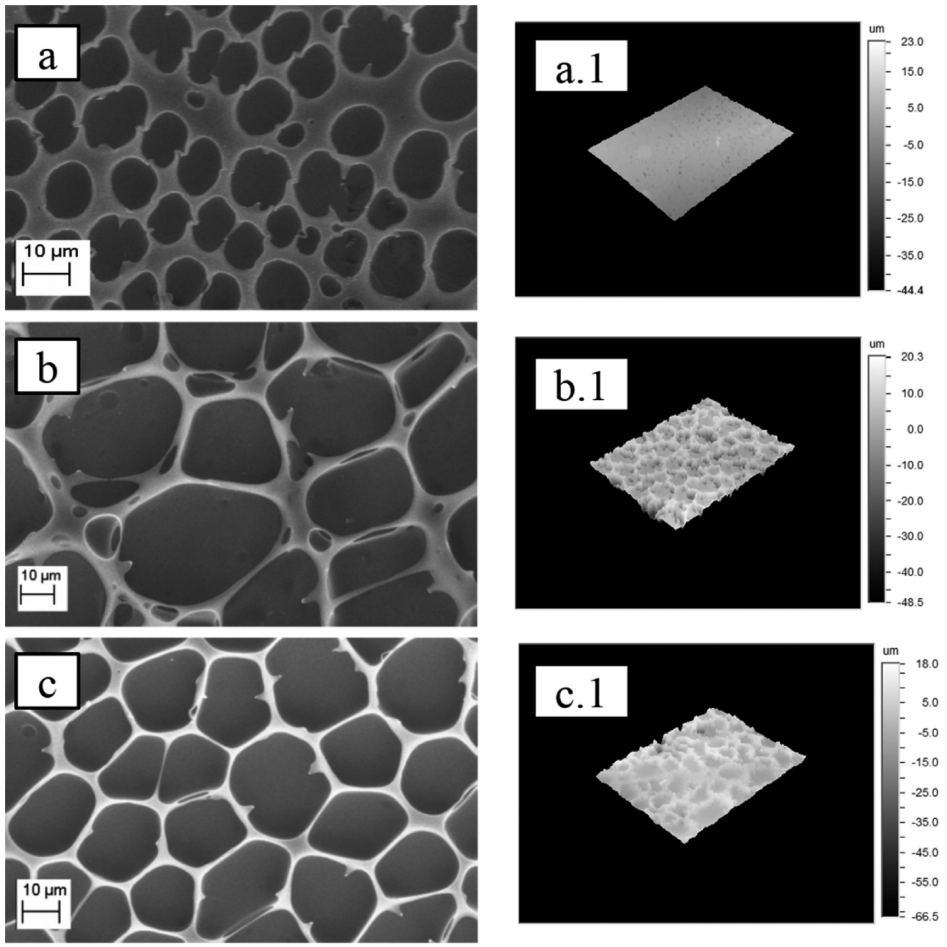

Figure 3. SEM and profilometry micrographs of scaffolds before and after nanoparticles incorporation: (a) PDLLA, (b) PDLLA/VACNT-O:nHAp1, and (c) PDLLA/VACNT-O:nHAp2 scaffolds. (a.1, b.1, and c.1) Profilometry micrographs.

to PDLLA scaffolds without incorporated nanoparticles (Figure 3a.1, control) was obtained. We associated this to more cavity formation after the nanoparticles incorporated into the PDLLA matrix. The PDLLA, PDLLA/VACNT-O:nHAp1, and PDLLA/VACNT-O:nHAp2 scaffolds showed porosity values at 84%, 60%, and 84%, respectively. The PDLLA scaffolds presented smaller pores on the surface (~227 pores) and 84% porosity. However, the PDLLA/VACNT-O:nHAp2 had 84% porosity with ~121 pores on the surface, probably due to greater absorption of nHAp2. We can attribute this to the higher porosity of nHAp1 produced by SBF method (Figure 2c.1).

Table 1 shows the surface roughness of the PDLLA, PDLLA/VACNT-O:nHAp1, and PDLLA/VACNT-O:nHAp2 scaffolds. We observed a significant difference between PDLLA (control) and PDLLA/VACNT-O:nHAp2 scaffolds. In comparison PDLLA/VACNT-O:nHAp2 scaffolds presented a roughness increase of 41.84%.

Table 1. Surface Roughness Analyses of the Different Scaffolds[a]

scaffolds	R_a (μm)	SD
PDLLA	4.11	0.32
PDLLA/VACNT-O:nHAp1	4.88	0.45
PDLLA/VACNT-O:nHAp2	5.83	0.94

[a]Data expressed as the average of three scaffolds (N = 3).

Figure 4a shows the surface energy analyses of PDLLA, PDLLA/VACNT-O:nHAp1, and PDLLA/VACNT-O:nHAp2 scaffolds after oxygen plasma treatment using polar and dispersive liquids. Data show that PDLLA scaffolds had a CA at 112°. However, there was a smaller difference in CA values after incorporation of nHAp1 nanoparticles into PDLLA scaffold structures (values between 89° and 112°). Clearly, a small control of CA was sufficient to improve the scaffold hydrophilicity. Several authors reported that a partially hydrophilic polymer surface with a contact angle of 60−90° enhances cell adhesion and that the surface energy can be related to cell adhesion on polymeric surfaces.[27−30] PDLLA and PDLLA/VACNT-O:nHAp1 scaffolds presented a lower difference in surface energy with values of 21.27 ± 5 mN m^{-1}. However, PDLLA/VACNT-O:nHAp2 scaffolds had a higher surface energy (27.35 ± 7 mN m^{-1}). We attributed this surface energy difference of PDLLA/VACNT-O:nHAp2 bioscaffolds to porous distribution control as shown in Figure 3c.

Figure 4b shows the collected ATR-FTIR spectra of PDLLA, PDLLA/VACNT-O:nHAp1, and PDLLA/VACNT-O:nHAp2 scaffolds. All of the groups presented a strong absorption band at 1750 cm^{-1} that corresponds to the carbonyl group (C−O) of the PDLLA chemical structure. Bands were observed at 1450 and 1380 cm^{-1}, assigned to a saturated absorption from the C−H bond, as well as a strong C−O absorption band at 1270−

DOI: 10.1021/acsami.5b01066
ACS Appl. Mater. Interfaces 2015, 7, 9385−9398

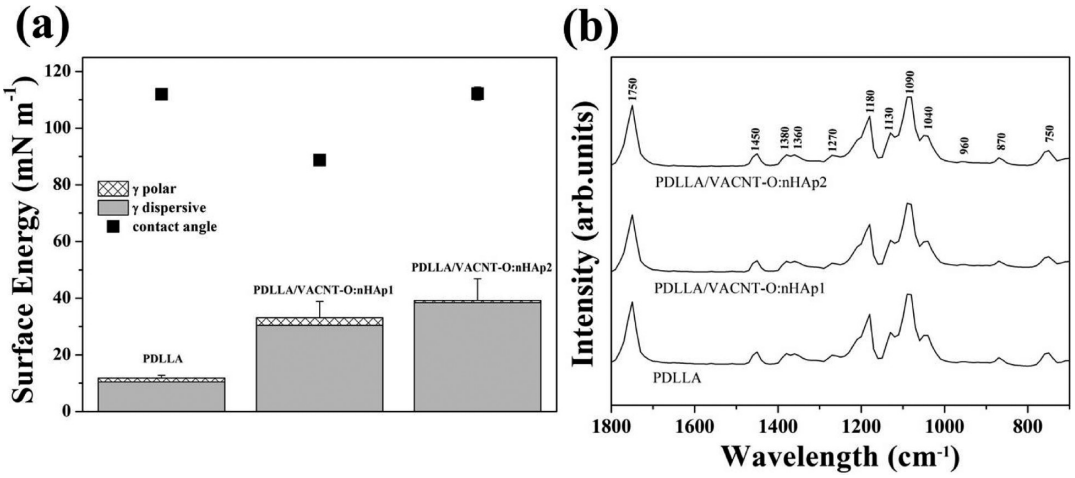

Figure 4. (a) Contact angle and surface energy analysis of all of the produced scaffolds with and without incorporated nanoparticles. We used PDLLA without nanoparticles as the control. Data were collected from three samples ($N = 3$). (b) AFT-FTIR spectra of PDLLA, PDLLA/VACNT-O:nHAp1, and PDLLA/VACNT-O:nHAp2 scaffolds. We collected all of the spectra in triplicate of three different points.

1045 cm^{-1}. The band at 750 cm^{-1} could be assigned to rocking ligation in -CH_2. The band at 870 cm^{-1} corresponds to deformation in the C−H bond, and the band at 960 cm^{-1} is assigned to CH═CH.[31−34]

We analyzed the peak area to prove the hydrophilic properties of the scaffolds after the oxygen plasma treatment. For this, we used the more intense peak centered at 1750 cm^{-1} attributed to the C−O bond. We observed an increase of 15% in area ($p < 0.05$) for both PDLLA/VACNT-O:nHAp1 and PDLLA/VACNT-O:nHAp2 scaffolds compared to PDLLA (control). We attributed this increase to the incorporation of oxygen groups after the plasma treatment.

The surface free energy components obtained with the Owens method[23] and interfacial free energies of adhesion calculated are listed in Table 2. We calculated the total surface energy by the sum of the polar (γ_p) and dispersive (γ_d) components.[25,26] We used thermodynamic expressions to estimate the dispersive and polar components, as well as the interfacial free energy of adhesion of scaffolds. We used the values of surface energy of L929 mouse fibroblast cell.[35,36] The data show that PDLLA has hydrophobic character with positive interfacial free energy of adhesion (ΔF_{adh}; Table 2). However, the scaffolds with incorporated nanoparticles were thermodynamically favorable to cell adhesion with ΔF_{adh} negative values.

Table 2. Surface Energy Components and Interfacial Free Energy of Adhesion of PDLLA, PDLLA/VACNT-O:nHAp1, and PDLLA/VACNT-O:nHAp2 Honeycomb Films

	surface free energy (mN m^{-1})			
scaffolds	γ_d [a]	γ_p [b]	total	F_{adh} (mJ m^{-2}) [c]
PDLLA	10.47	1.38	11.85	20.4
PDLLA/VACNT-O:nHAp1	30.42	2.7	33.12	−5.3
PDLLA/VACNT-O:nHAp2	38.42	0.78	39.2	−10.2

[a] γ_d, dispersive. [b] γ_p, polar. [c] F_{adh}, interfacial free energy of adhesion.

Figure 5a shows thermograms of PDLLA scaffolds with and without incorporated nanoparticles, and Figure 5b shows thermogravimetric analysis. Table 3 shows thermal parameters calculated from these thermograms.

The first endothermic peak, between 55 and 69 °C, was attributed to residual solvent evaporation. Because the range of evaporation of the residual solvent was in the same range as the PDLLA glass transition temperature, this last one was not measured. The composite materials had a small amount of residual solvent. For PDLLA, PDLLA/VACNT-O:nHAp1, and PDLLA/VACNT-O:nHAp2 scaffolds this quantity was 2.4%, 3.4%, and 2.5% (w/w), respectively. Organic solvents are harmful for cell growth: however, this amount can be evaporated by leaving the materials in a kiln at 60 °C before their use as scaffolds for bone regeneration. We observed in PDLLA/VACNT-O:nHAp2 scaffolds two endothermic peaks at 58 and 62 °C. We related it to the remaining SBF and chloroform evaporation in the scaffolds structure. The exothermic peak was attributed to the cold crystallization process during the DSC heating run. The addition of VACNT-O:nHAp (nHAp1 and nHAp2) depressed the t_c of scaffolds when compared to neat PDLLA, indicating that PDLLA/VACNT-O:nHAp scaffolds probably act as a nucleating agent increasing the crystallization rate in the neat PDLLA. Increases in the enthalpy of melting, in both scaffolds, confirm the nucleating role of nanofiller in the cold crystallization process, also observed by other researchers.[37,38] A longer crystallization time (lower t_c values) may induce a larger occurrence of crystal perfection, increasing the enthalpy (ΔH_m), temperature of melting (T_m), and crystallinity (X_c)[39] (Table 3). We showed that the VACNT-O:nHAp1 and VACNT-O:nHAp2 scaffolds improved the PDLLA crystallinity (X_c). Higher crystallinity leads to enhanced precipitation of apatite over the VACNT-O surface and may help osteoblast cell attachment onto the scaffolds.[40]

Figure 5b shows the thermogravimetric analyses characterizing the mass losses of PDLLA, PDLLA/VACNT-O:nHAp1, and PDLLA/VACNT-O:nHAp2 scaffolds. The three samples presented very similar thermal behavior when exposed to the same heating ratios. All samples, when exposed to a heating rate of 20 °C min^{-1}, showed mass loss at equivalent temperatures, meaning that the addition of nanoparticles did not alter the resistance to thermal decomposition.

Parts a−c of Figure 6 present the SEM micrographs collected from PDLLA, PDLLA/VACNT-O:nHAp1, and PDLLA/VACNT-O:nHAp2 scaffolds after soaking in SBF for 14 days.

DOI: 10.1021/acsami.5b01066
ACS Appl. Mater. Interfaces 2015, 7, 9385−9398

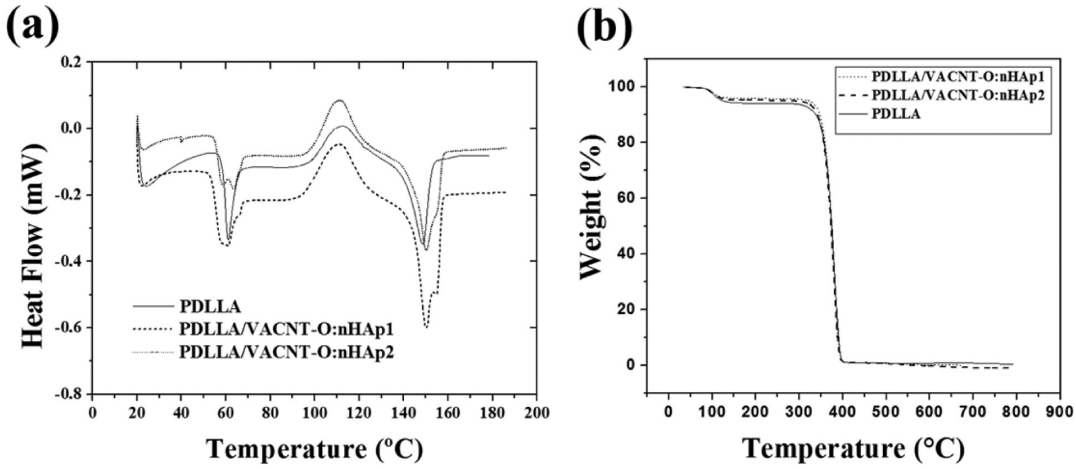

Figure 5. (a) Thermograms obtained by differential scanning calorimetry of the PDLLA, PDLLA/VACNT-O:nHAp1, and PDLLA/VACNT-O:nHAp2 bioscaffolds and (b) thermogravimetric analyses of the PDLLA, PDLLA/VACNT-O:nHAp1, and PDLLA/VACNT-O:nHAp2 scaffolds.

Table 3. Thermal Parameters of PDLLA and Produced PDLLA/VACNT-O:nHAp Scaffolds

scaffold	ΔH_v (J g^{-1})	ΔH_{cc} (J g^{-1})	ΔH_m (J g^{-1})	T_{cc} (°C)	T_m (°C)	X_c (%)
PDLLA	6.7	12.4	13.6	112.2	148.7	13.5
PDLLA/VACNT-O:nHAp1	9.2	18.2	23.4	111.3	150.2	23.2
PDLLA/VACNT-O:nHAp2	6.5	15.3	18.3	111.3	150.1	18.1

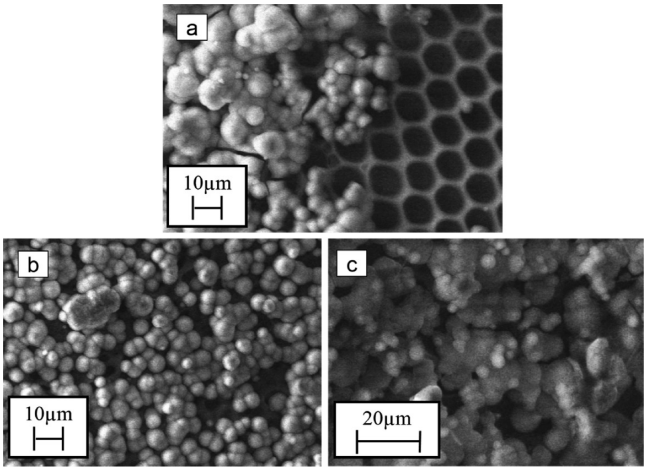

Figure 6. Typical scanning electron micrographs of (a) PDLLA, (b) PDLLA/VACNT-O:nHAp1, and (c) PDLLA/VACNT-O:nHAp2 scaffolds after the biomineralization process.

In general, the scaffolds presented bioactivity properties. However, we observed several differences between the scaffold groups. We showed that the PDLLA VACNT-O:nHAp1 and VACNT-O:nHAp2 scaffolds presented more pores and roughness than PDLLA scaffolds. These surface properties directly contributed to bioactivity properties. PDLLA scaffolds had a nonhomogeneous globular apatite layer (Figure 6a). We clearly observed a compact globular nHAp layer on VACNT-O:nHAp1 (Figure 6b) and VACNT-O:nHAp2 (Figure 6c) bioscaffolds after 15 days soaking in SBF.

We proved the bioactivity and biomineralization process of all of the produced scaffolds using the ATR-FTIR analysis (Figure 7a). All of the scaffold groups had a strong absorption band at 1750 cm^{-1} that corresponds to the carbonyl group (C−O) of the PDLLA.[41] Data show the peak at 960 cm^{-1}, attributed to phosphate stretch mode, identifying the carbonated nHAp presence, and the absorption band of the phosphate groups are found between 1200 and 1030 cm^{-1}.[42−45] The bands in region of 1300−1650 cm^{-1} and that at 870 cm^{-1} are designated to carbonate in the surface.[42−45] We can observe that the areas of phosphate and carbonate bands were increased in the control group, which occurred probably due to the smaller diameter of surface pores obtained by the control group. Nanosized pores can also act as sites for starting nucleation and apatite crystals growth.[46]

In addition, we obtained approximate values of CO_3^{2-}/PO_4^{3-} ratios, which proved the bioactivity and biomineralization for all of the bioscaffolds (Table 4). The incorporation of nanoparticles in the polymeric matrix aimed to improve the osteointegration process during the polymer degradation.

Figure 7b shows the characterization of PDLLA, PDLLA/VACNT-O:HAp1, and PDLLA/VACNT-O:nHAp2 scaffolds after soaking in SBF for 14 days. It is possible to identify the typical peaks for carbonated nHAp, crystallographic reference JCPDS 019-0272, on 25.7° (002), 29.3° (210), 32.2° (112), 39.4° (212), 47.1° (222), 49.5° (213), and 52.7° (004).

The most intense peaks observed in the PDLLA/VACNT-O:nHAp2 scaffolds suggested higher calcium precipitation and subsequently a thicker layer formation of carbonated nHAp, resulting in an increased crystallinity compared to the other scaffolds with larger peaks.

Table 5 shows details about X-ray diffraction peaks, full width at half-maximum (fwhm) calculated from X-ray diffraction peaks, and calculated crystallite size. An increase of crystallite size in PDLLA/VACNT-O:nHAp2 scaffolds clearly occurred compared to other produced scaffolds. The incorporation of carbonate nHAp and the active sites formation for nucleation during the precipitation/dissolution reaction was further indicated.[46,47]

The biomineralization on the material surface is an indicator of bone bioactivity, and it is the first *in vitro* method for testing the applicability of a material to bone tissue regeneration.[47]

DOI: 10.1021/acsami.5b01066
ACS Appl. Mater. Interfaces 2015, 7, 9385−9398

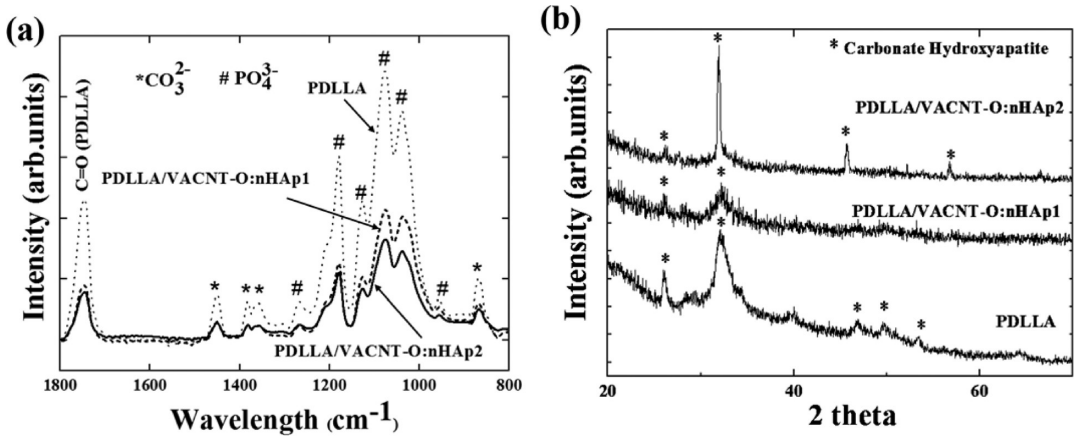

Figure 7. (a) ATR-FTIR spectra collected from PDLLA, PDLLA/VACNT-O:nHAp1, and PDLLA/VACNT-O:nHAp2 scaffolds after soaking in simulated body fluid for 14 days; (b) X-ray difractogram patterns of PDLLA, PDLLA/VACNT-O:nHAp1, and PDLLA/VACNT-O:nHAp2 scaffolds after soaking in SBF for 14 days.

Table 4. Carbonate/Phosphate Ratio Collected from the Fourier Transform Infrared Spectra on PDLLA, PDLLA/VACNT-O:nHAp1, and PDLLA/VACNT-O:nHAp2 Scaffolds

scaffold	CO_3^{2-}/PO_4^{3-}
PDLLA	0.061
PDLLA/VACNT-O:nHAp1	0.063
PDLLA/VACNT-O:nHAp2	0.059

Table 5. Crystallite Size of PDLLA, PDLLA/VACNT-O:nHAp1, and PDLLA/VACNT-O:nHAp2 Scaffolds after Soaking in SBF for 14 days

scaffold	2θ peak (deg)	2θ fwhm	crystallite size (Å)
PDLLA	31.9	0.47	177
PDLLA/VACNT-O:nHAp1	32.2	0.94	88
PDLLA/VACNT-O:nHAp2	32.0	0.13	617

Figure 8 summarizes *in vitro* biological assays using osteoblasts. Figure 8a showed that all of the produced scaffolds

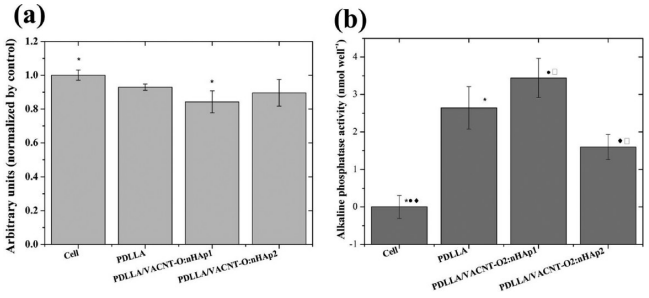

Figure 8. Cell viability (a) and alkaline phosphatase (b) assays of PDLLA, PDLLA/VACNT-O:nHAp1, and PDLLA/VACNT-O:nHAp2 scaffolds. Osteoblasts were cultivated for 5 days on the scaffolds.

presented low cytotoxic, keeping the viability close to that observed for the control group. Analysis of variance indicated differences between groups ($p = 0.04113$), and the Tukey's post hoc test pointed to differences between the cell positive control and the PDLLA/VACNT-O:nHAp1 scaffold group. Figure 8b shows the ALP assay. This assay suggested that all produced scaffolds were able to induce detectable mineralization effect. It is due to the measured alkaline phosphatase activity when compared to the positive control (only cells) as a basal value. Differences were statistically found among the groups ($p = 0.00007$). Tukey's testing pointed to differences between PDLLA/VACNT-O:nHAp1 scaffolds when compared to PDLLA/VACNT-O:nHAp2, and all produced scaffolds differed from the control.

Our *in vitro* results suggested the biocompatibility of all produced scaffolds, because viability levels were above 80% when compared to the positive control (cells). Viability assessment with SRB has been described in the literature,[48,49] with the advantage that it does not rely on the ability of cells in metabolizing a salt. In fact, it is related to the staining and quantification of cell proteins, to provide a direct correlation between the amount of proteins and the number of cells. The PDLLA/VACNT-O:nHAp1 scaffolds were found to be less biocompatible or, at least, to induce a decreased cell growth when compared to the control group. Interestingly, these data could be directly correlated with the alkaline phosphatase activity, where the PDLLA/VACNT-O:nHAp1 scaffolds group had a significant increase on the enzyme activity. In our test with the mineralization media, the same pattern was observed: a significant increase in ALP activity was also correlated to a decrease in cell count with SRB (data not shown). This can directly indicate that the PDLLA/VACNT-O:nHAp1 scaffolds group also induces a higher level of cell differentiation, favoring mineralization and decreasing cell growth at first contact with the cells.

We implanted in a rat calvarium defect the PDLLA, PDLLA/VACNT-O:nHAp1, and PDLLA/VACNT-O:nHAp2 scaffolds. Figure 9 shows typical histological sections after 4 months of implantation. In general, our data encouraged the application of PDLLA/VACNT-O:nHAp biooscaffolds for bone tissue regeneration. We demonstrated biocompatibility of PDLLA scaffolds because of the noninflammation process after their implantation. The PDLLA scaffolds showed a low rate of absorption despite the fibroblast in PDLLA. The adjacent tissue had basophilic colored tissue, with prolonged nucleus close to each other as an aspect of fibrosis, still showing a tissue with incomplete recovery (parts a and a.1 of Figure 9). Figure 9b neatly illustrates the interface region between the bioscaffolds and bone with multinucleated osteoclasts digging into the

DOI: 10.1021/acsami.5b01066
ACS Appl. Mater. Interfaces 2015, 7, 9385−9398

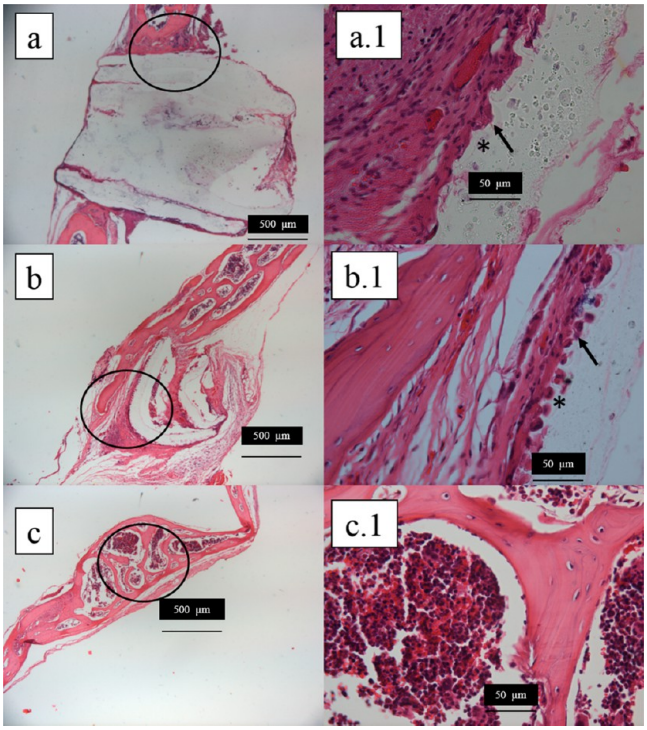

Figure 9. Photomicrograph of histological slides identifying bone regeneration after 4 months of implant in groups: (a) bone regeneration after implantation of PDLLA scaffolds as control (H&E, 40×); (a.1) details in circles (H&E, 100×; interface region between the polymer and bone (*) and arrow indicates fibroblast); (b) bone regeneration after implantation of PDLLA/VACNT-O:nHAp1 scaffolds (H&E, 40×); (b.1) interface region between the polymer and bone (*), which resembles the Howship's lacunae formed by osteoclasts in arrows (H&E, 100×); (c) complete bone regeneration after implantation of PDLLA/VACNT-O:nHAp2 scaffolds (H&E, 40×); (c.1) MB indication of the formation of bone marrow (H&E, 100×).

PDLLA/VACNT-O:nHAp1 scaffolds presenting structures that resembled Howship's lacunae. We observed the presence of an acidophilic adjacent tissue featuring the osseous matrix (arrow) as well as a process of tissue recovery (Figure 9b.1). The PDLLA/VACNT-O:nHAp1 scaffolds had a better rate of absorption than PDLLA scaffolds (Figure 9a.1). In PDLLA/VACNT-O:nHAp2 scaffolds (Figure 9c), we obtained the best results when compared to the PDLLA and PDLLA/VACNT-O:nHAp1 scaffolds. Complete healing of the defect was observed, with a wider and no-strait bone formation due to osseous callus. The newly formed bone was precisely organized, including delimited marrow space, without any signal of scaffold material or poor bone formation (Figure 9c.1).

The native bone tissue comprises a highly specialized structure at the molecular level, organized by organic and inorganic macromolecules with important chemical properties required for tissue function. The biomimetic modification supports the cells in the recognition of the material, improving target functions such as cell adhesion and proliferation.[50] The presence of nHAp crystals in PDLLA scaffolds increased the bone healing process in both PDLLA/VACNT-O:nHAp1 and PDLLA/VACNT-O:nHAp2 scaffolds. However, the complete polymer bio-reabsorption and structural bone formation was accomplished only in the implanted PDLLA/VACNT-O:nHAp2 scaffolds. Intrinsic characteristics of the material, such as thickness of PDLLA scaffolds, size of the pores, and crystallinity of carbonate hydroxyapatite, may have contributed to the success of bone regeneration by this particular biomaterial. This agrees with our previous results regarding biocompatibility and osteoinduction in globular nanoparticles.[16]

The SEM analysis complements the histological results (Figure 10). The PDLLA scaffolds were not degraded (Figure 10a.1). The PDLLA/VACNT-O:nHAp1 scaffolds were partially degraded and formed a biological apatite layer on the surface confirming the bioactivity results *in vitro* (Figure 10b). Figure 10b.1 shows details of partially degraded polymer (*) and carbonated hydroxyapatite layer (arrow). Figure 10c shows the complete bone repair and degradation of the PDLLA/VACNT-O:nHAp2 scaffolds, and the formation of apatite layer proves the results in Figure 10c.1 with details of osteoblasts (square) in the bone tissue.

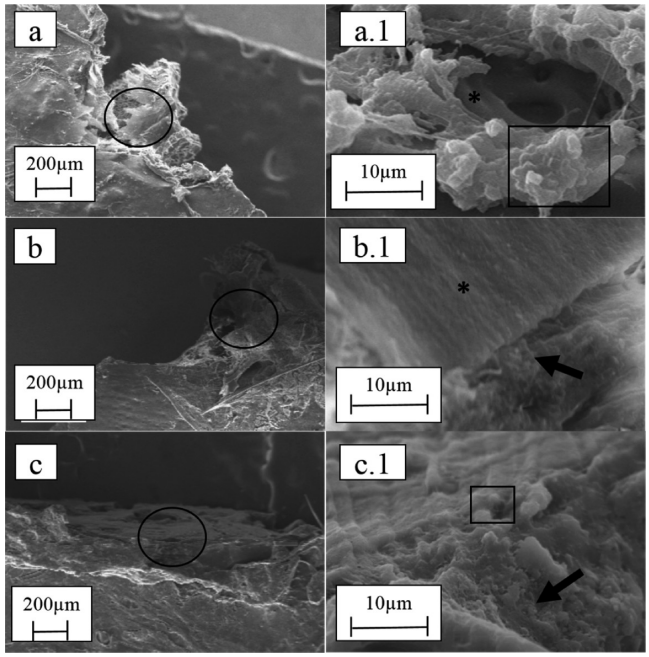

Figure 10. SEM micrographs of bone identifying bone regeneration 4 months after implantation in groups: (a) bone regeneration after implantation of PDLLA scaffolds as control; (a.1) detail in circled area of panel a of interface region between the polymer and bone (*) and arrow indicating macrophages; (b) bone regeneration after implantation of PDLLA/VACNT-O:nHAp1 scaffolds; (b.1) detail of partially degraded polymer (*) and carbonated hydroxyapatite layer (arrow); (c) bone complete regeneration after implantation of PDLLA/VACNT-O:nHAp2 scaffolds; (c.1) detail of osteoblasts (square) and carbonated hydroxyapatite layer (arrow).

In this work, we obtained 3D porous polymeric honeycomb scaffolds that do not alter the thermal degradation properties of PDLLA. The incorporation of VACNT-O and nHAp into the polymer matrix resulted in an osteoconductive biomaterial.[51,52]

We associated an optical technique for interface between bone growth and the implantable region. Figure 11 shows the confocal Raman results collected from the interface of the bone defect and PDLLA, PDLLA/VACNT-O:nHAp1, and PDLLA/VACNT-O:nHAp2 scaffolds. Bands were observed at $\upsilon 2$ phosphate at 431−433 cm^{-1}, $\upsilon 4$ phosphate at 584−589 cm^{-1}, proline at 855−857 cm^{-1}, $\upsilon 1$ phosphate at 960 cm^{-1}, phenylamine at 1005 cm^{-1}, carbonate at 1071−1072 cm^{-1},

DOI: 10.1021/acsami.5b01066
ACS Appl. Mater. Interfaces 2015, 7, 9385−9398

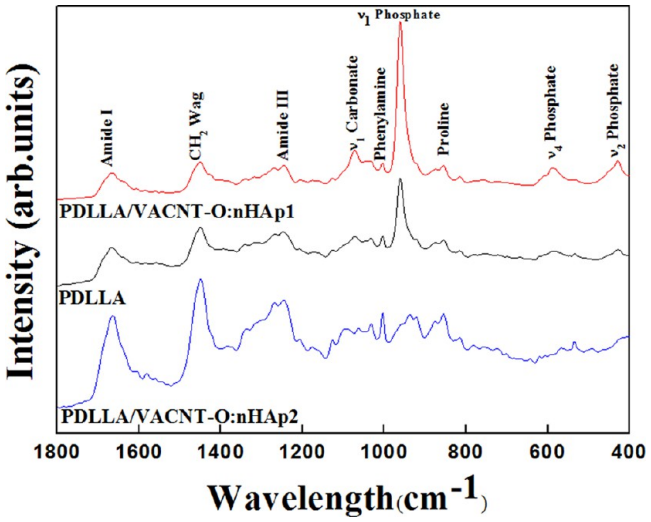

Figure 11. Representative Raman spectrum collected from bone section after 4 months with incorporated PDLLA, PDLLA/VACNT-O:nHAp1, and PDLLA/VACNT-O:nHAp2 scaffolds.

amide III at 1247−1248 cm^{-1}, CH_2-wag at 1451−1452 cm^{-1}, and amide I at 1666−1667 cm^{-1}.[47−49,53−56]

In this study, the Raman peak areas corresponding to the carbonate and phosphate were calculated to quantify the difference of biomineralization between the interface of formed bone and scaffolds. Thus, the phosphate/proline, phosphate/amide III, phosphate/amide I, and carbonate/amide I values were related to the degree of mineralization, which is characterized by the ratio between mineral and organic matrix composite.[57−60]

Table 6 shows calculated fwhm from confocal Raman peaks of phosphate (PO_4^{3-}) and carbonate (CO_3^{2-}) vibrational modes, and PO_4^{3-}/CO_3^{2-} ratios. Clearly an fwhm increase occurs of the matrix mineral components to implanted PDLLA/VACNT-O:nHAp1 scaffolds; calcium and phosphate are responsible for rigidity and mechanical properties.

Table 6. Comparison of Phosphate (PO_4^{3-}) and Carbonate (CO_3^{2-}) fwhm Peak Values of PDLLA and PDLLA/VACNT-O:nHAp1 Scaffolds (fwhm; R^2, 0.99) Collected from Bone Section Extracted after 4 Months[a]

scaffold	PO_4^{3-}	CO_3^{2-}	CO_3^{2-}/PO_4^{3-}
PDLLA	24	19	0.79
PDLLA/VACNT-O:nHAp1	34	21	0.62

[a]We also included PO_4^{3-}/CO_3^{2-}. The groups are significantly different, $p < 0.05$ (One Way Anova).

In the process of bone formation, the first mineralization is intrafibrillar and then the interfibrillar occurs. Minerals intrafibrillarly occupy about 30−40% of the volume, whereas an average mineral of human bone has 50−60% around the collagen fiber,[61] but the mineral bone composition can reach 60−70% of dry bone weight.[62]

Table 7 shows different proteins' ratio contents collected from bone section extracted from the region of implant after 4 months. The values displayed in Table 7 indicate an increase in the mineralization process in bone regeneration using PDLLA/VACNT-O:nHAp1 scaffolds compared to the control group. The PDLLA/VACNT-O:nHAp1 scaffolds promote mineralization with an increased proportion of minerals in the matrix. This difference in the chemical composition of bone formed at the interface with the biomaterial may be a consequence of osteoinduction due to nHAp1 obtained by electrodeposition. The replacement of carbonate is indicative of bone quality.[57,58] The lower ratio of carbonate precipitation on PDLLA/VACNT-O:nHAp1 scaffolds, as well as an increase in the ratios of mineralization to organic content of the matrix, indicates a better quality of bone tissue.

The spectra analyses of PDLLA/VACNT-O:nHAp2 scaffolds show no functional groups' constituent related to the mineralized matrix. The profile of the organic matrix spectrum with bands assigned to collagen[62]suggests the formation of periosteal callus and the occlusion of the bone wound.[63]

Mikael et al.[64] reported the production of three-dimensional porous PLGA membranes by incorporating MWCNTs, and the dispersed MWCNTs favored attachment and cell proliferation as well as improved mechanical properties of PLGA. In conclusion, the three-dimensional membranes produced by Mikael et al. are promising biomaterials for bone regeneration.[64] Deplaine et al. evaluated PDLLA/HAp scaffolds produced by *in situ* polymerization method. The initial responses showed grade I cytotoxicity according to the standard ISO 109931. There were no cases of animal death, only a small inflammatory response in 1−9 weeks.[65] Our *in vitro* results showed no cytotoxicity, and all animals' survived exposure for 4 months. Deplaine et al. reported that the plasma treatment and HAp incorporation into the polymer improves nucleation in SBF, forming a thicker layer of biological apatite. This material when implanted in osteochondral lesions of sheep promoted the appearance of osteoid similar to mature bone.[66]

Van der Zande et al. reported the production of polymeric scaffolds with the incorporation of CNT and HAp for improving the mechanical properties, osteoconductivity, and bone morphogenetic protein-2 (BMP-2) retention onto the scaffold. These authors evaluated the release of BMP-2 of PLLA-CNT-μHAp scaffolds up to 5 weeks in rats and also found that the incorporation of nanoparticles did not alter the bioactivity of BMP2.[67] Mahjoubi et al. studied PDLLA surface modification to obtain hydrophilic character using diazonium method to improve the biomineralization and cell growth on PDLLA modified surface, respectively.[68] Hasegawa et al. implanted PDLLA/HAp scaffolds in the femoral intercondylar notch and, after 26 weeks, found increased bone formation and

Table 7. Comparison of Phosphate/Proline, Phosphate/Amide III, Phosphate/Amide I, and Carbonate/Amide I Ratios of PDLLA and PDLLA/VACNT-O:nHAp1 Scaffolds (fwhm; R^2, 0.99) Collected from Bone Section Extracted from Region Implant after 4 Months[a]

scaffold	phosphate/proline	phosphate/amide III	phosphate/amide I	carbonate/amide I
PDLLA	1.49	0.65	0.79	0.63
PDLLA/VACNT-O:nHAp1	2.17	2.02	1.60	0.99

[a]The groups are significantly different, $p < 0.05$ (One Way Anova).

DOI: 10.1021/acsami.5b01066
ACS Appl. Mater. Interfaces 2015, 7, 9385−9398

PDLLA/HAp scaffolds showed faster degradation than the HAp control.[52] The degradation time of the amorphous PDLLA scaffolds occurred at 72 weeks.[69] Our results showed that the crystalline biomimetic apatite produced after soaking VACNT-O in SBF (nHAp2 group) and incorporated into the PDLLA scaffolds contributes to accelerating polymer degradation; the PDLLA/VACNT-O:nHAp2 scaffolds were completely degraded after 4 months.

4. CONCLUSION

For the first time, we have demonstrated an association between *in vitro* and *in vivo* studies of the PDLLA scaffolds with different incorporated VACNT-O:nHAp nanoparticles produced by electrodeposition and immersion into SBF solution. Our *in vitro* results showed that the produced scaffolds simultaneously promote bioactivity without any cytotoxic effects. *In vivo* study showed that the PDLLA/VACNT-O:nHAp2 scaffolds mimicked the immature bone and induced bone remodeling. The PDLLA/VACNT-O:nHAp scaffolds presented superior morphology and porosity properties compared to the PDLLA alone. These findings indicate surface improvement and the applicability of this new nanobiomaterial for bone regenerative medicine.

AUTHOR INFORMATION

Corresponding Author

*Phone: +55 12 3947-1100. Fax: +55 12 3947-6717. E-mail: lobo.aol@gmail.com; aolobo@pq.cnpq.br.

Author Contributions

[#]I.A.W.B.S. and A.O.L. contributed equally.

Notes

The authors declare no competing financial interest.

ACKNOWLEDGMENTS

We thank the Sao Paulo Research Foundation (FAPESP; Grants 2011/17877-7, 2011/20345-7, and 2012/02159-4), Brazilian Innovation Agency (FINEP Grant 01-13-0428-00 / ref. no. 1259/13), National Council for Scientific and Technological Development (CNPq Grants 474090/2013-2 and 307809/2013-7) and Coordination for the Improvement of Higher Education Personnel (CAPES) for financial support. We thank Purac for kindly providing the PDLLA (grade, 9/04 (m/m), Purasorb; Puracbiochem, Gorinchem, Holland).

ABBREVIATIONS

ALP = alkaline phosphatase
ATR-FTIR = reflection Fourier transform infrared
CA = contact angle
$CaCl_2 \cdot 2H_2O$ = calcium chloride dihydrate
$Ca(NO_3)_2 \cdot 4H_2O$ = calcium nitrate tetrahydrate
CNT = carbon nanotubes
DSC = differential scanning calorimetry
JCPDS = The International Centre for Diffraction Data
$MgCl_2 \cdot 6H_2O$ = magnesium chloride hexahydrate
MWCVD = microwave plasma chamber
$Na_2HPO_4 \cdot 2H_2O$ = disodium phosphate
NaCl = sodium chloride
$NaHCO_3$ = sodium bicarbonate
$(NH_4) \cdot 2HPO_4$ = ammonium hydrogen phosphate
nHAp = nanohydroxyapatite
nHAp1 = nHAp crystals directly electrodeposited onto VACNT-O
nHAp2 = VACNT-O soaked in SBF solution to produce nHAp crystals
PDLLA = poly(D,L-lactide acid)
PDLLA/VACNT-O:nHAp = PDLLA/superhydrophilic vertically aligned carbon nanotubes:nanohydroxyapatite/
PLLA = poly(lactic acid)
SBF = simulated body fluid
SEM = scanning electron microscope
SRB = sulforodhamine B
t_c = crystallization time
T_g = glass transition temperature
T_m = temperature of melting
VACNT-O = superhydrophilic vertically aligned CNT
X_c = crystallinity
γ_p = polar component
γ_d = dispersive component
ΔF_{adh} = interfacial adhesion energy
ΔH_m = enthalpy

REFERENCES

(1) An, Y. H.; Woolf, S. K.; Friedman, R. J. Pre-clinical in Vivo Evaluation of Orthopaedic Bioabsorbable Devices. *Biomaterials* **2000**, *21*, 2635−2652.
(2) Tian, H.; Tang, Z.; Zhuang, X.; Chen, X.; Jing, X. Biodegradable Synthetic Polymers: Preparation, Functionalization and Biomedical Application. *Prog. Polym. Sci.* **2012**, *37*, 237−280.
(3) Merolli, A.; Gabbi, C.; Cacchioli, A.; Ragionieri, L.; Caruso, L.; Giannotta, L.; Tranquilli, L. P. Bone Response to Polymers Based on Poly-lactic Acid and Having Different Degradation Times. *J. Mater. Sci.: Mater. Med.* **2011**, *12*, 775−778.
(4) Chen, C.; Chueh, J.; Tseng, H.; Huang, H.; Lee, S. Preparation and Characterization of Biodegradable PLA Polymeric Blends. *Biomaterials* **2003**, *24*, 1163−1173.
(5) Alves, C. M.; Yang, Y.; Marton, D.; Carnes, D. L.; Ong, J. L.; Sylvia, V. L.; Dean, D. D.; Reis, R. L.; Agrawal, C. M. J. Plasma Surface Modification of Poly (D,L-lactic acid) as a Tool to Enhance Protein Adsorption and the Attachment of Different Cell Types. *J. Biomed. Mater. Res.* **2008**, *87* (PartB), 59−66.
(6) Nair, L. S.; Laurencin, C. T. Biodegradable Polymers as Biomaterials. *Prog. Polym. Sci.* **2007**, *32*, 762−798.
(7) Eggers, C.; Meeder, P. J. Biological Principles of Autogenous Bone Grafting. *Injury* **1994**, *25*, 17−20.
(8) Nade, S. Stimulating Osteogenesis. *Injury* **1994**, *25*, 577−583.
(9) Liu, Y.; Li, X.; Zou, B.; Chen, J.; Cai, Z.; Qua, S.; Zhu, M.; Qian, L. Fretting Behaviors of Hot-Pressed Electrospun Hydroxyapatite/Poly(dl-lactide) Fibrous Composites as Potential Orthopedic Implants. *Tribol. Int.* **2012**, *53*, 124−133.
(10) Zheng, X.; Zhou, S.; Li, X.; Weng, J. Shape Memory Properties of Poly(D,L-lactide)/Hydroxyapatite Composites. *Biomaterials* **2006**, *27*, 4288−4295.
(11) Shao, S.; Zhou, S.; Li, L.; Li, J.; Luo, C.; Wang, J.; Li, X.; Weng, J. Osteoblast Function on Electrically Conductive Electrospun PLA/MWCNTs Nanofibers. *Biomaterials* **2011**, *32*, 2821−2833.
(12) Lobo, A. O.; Corat, M. A. F.; Antunes, E. F.; Ramos, S. C.; Pacheco-Soares, C.; Corat, E. J. Cytocompatibility Studies of Vertically-aligned Multi-walled Carbon Nanotubes: Raw Material and Functionalized by Oxygen Plasma. *Mater. Sci. Eng., C* **2012**, *32*, 648−652.
(13) Lobo, A. O.; Corat, M. A. F.; Ramos, A. C.; Matsushima, J. T.; Granato, A. E. C.; Pacheco-Soares, C.; Corat, E. J. Fast Preparation of Hydroxyapatite/Superhydrophilic Vertically Aligned Multiwalled Carbon Nanotube Composites for Bioactive Application. *Langmuir* **2010**, *26*, 18308−18314.
(14) Lobo, A. O.; Marciano, F. R.; Regiani, I.; Ramos, S. C.; Matsushima, J. T.; Corat, E. J. Proposed Model for Growth Preference of Plate-like Nanohydroxyapatite Crystals on Superhydrophilic

DOI: 10.1021/acsami.5b01066
ACS Appl. Mater. Interfaces 2015, 7, 9385−9398

Vertically Aligned Carbon Nanotubes by Electrodeposition. *Theor. Chem. Acc.* **2011**, *130*, 1071−1082.
(15) Lobo, A. O.; Siqueira, I. A. W. B.; Neves, M. F.; Marciano, F. R.; Corat, E. J.; Corat, M. A. F. In Vitro and in Vivo Studies of a Novel Nanohydroxyapatite/Superhydrophilic Vertically Aligned Carbon Nanotube Nanocomposites. *J. Mater. Sci.: Mater. Med.* **2013**, *24*, 1723−1732.
(16) Marsi, T. C. O.; Corat, M. A. F.; Machado, M. M.; Corat, E. J.; Marciano, F. R.; Lobo, A. O. Correlation and Comparison between Thermodynamic Aspects and Cytocompatibility of Cells on Superhydrophobic and Superhydrophilic Vertically Aligned Carbon Nanotubes. *Curr. Phys. Chem.* **2012**, *3*, 155−165.
(17) Barrere, F.; van Blitterswijk, C. A.; de Groot, K.; Layrolle, P. Nucleation of Biomimetic Ca-P Coatings on Ti6Al4V from a SBFX5 Solution: Influence of Magnesium. *Biomaterials* **2002**, *23*, 2211−2220.
(18) Barrere, F.; van Blitterswijk, C. A.; de Groot, K.; Layrolle, P. Influence of Ionic Strength and Carbonate on the Ca-P Coating Formation from SBF×5 Solution. *Biomaterials* **2002**, *23*, 1921−1930.
(19) Sunamia, H.; Ito, E.; Tanaka, M.; Yamamoto, S.; Shimomura, M. Effect of Honeycomb Film on Protein Adsorption, Cell Adhesion and Proliferation. *Colloids Surf., A* **2006**, *284*−*285*, 548−551.
(20) Lobo, A. O.; Marciano, F. R.; Ramos, S. C.; Machado, M. M.; Corat, E. J.; Corat, M. A. F. Increasing Mouse Embryonic Fibroblast Cell Adhesion on Superhydrophilic Vertically Aligned Carbon Nanotube Films. *Mater. Sci. Eng., C* **2011**, *31*, 1505−1511.
(21) Cai, K.; Yao, K.; Lin, S.; Yang, Z.; Li, X.; Xie, H.; Qing, T.; Gao, L. Poly(d,l-lactic acid) Surfaces Modified by Silk Fibroin: Effects on the Culture of Osteoblast in Vitro. *Biomaterials* **2002**, *23*, 1153−1160.
(22) Wang, X.; Zhang, L.; Sun, D.; An, Q.; Chen, H. Formation Mechanism and Crystallization of Poly(vinylidene fluoride) Membrane Via Immersion Precipitation Method. *Desalination* **2009**, *236*, 170−178.
(23) Neto, W. A. R.; Pereira, I. H. L.; Ayres, E.; Paula, A. C. C.; Averous, A. M. G.; Oréfice, R. L.; Bretas, R. E. S. B. Influence of the Microstructure and Mechanical Strength of Nanofibers of Biodegradable Polymers with Hydroxyapatite in Stem Cells Growth. Electrospinning, characterisation and Cell Viability. *Polym. Degrad. Stab.* **2012**, *97*, 2037−2051.
(24) Owens, D. K.; Wendt, R. C. Estimation of the Surface Free Energy of Polymers. *J. Appl. Polym. Sci.* **1969**, *13*, 1741−1747.
(25) Van Oss, C. J.; Good, R. J.; Chaundhury, M. K. The Role of van der Waals Forces and Hydrogen Bonds in "Hydrophobic Interaction" between Biopolymers and Low Energy Surfaces. *J. Colloid Interface Sci.* **1986**, *111*, 378−390.
(26) Schender, R. P. Conditioning Film- Induced Modification of Substratum Physicochemistry—Analysis by Contact Angles. *J. Colloid Interface Sci.* **1996**, *182*, 204−213.
(27) Tamada, Y.; Ikada, Y. Fibroblast Growth on Polymer Surfaces and Biosynthesis of Collagen. *J. Biomed. Mater. Res.* **1994**, *28*, 783−789.
(28) Ikada, Y. Surface Modification of Polymers for Medical Applications. *Biomaterials* **1994**, *15*, 726−736.
(29) Van Wachem, P.; Hogt, A.; Beugeling, T.; Feijen, J.; Bantjes, A.; Detmers, J.; van Aken, W. Adhesion of Cultured Human Endothelial Cells onto Methacrylate Polymers with Varying Surface Wettability and Charge. *Biomaterials* **1987**, *8*, 323−328.
(30) Hasson, J.; Wiebe, D.; Abbott, W. Adult Human Vascular Endothelial Cell Attachment and Migration on Novel Bioabsorvable Polymers. *AMA Arch. Surg.* **1987**, *122*, 428−430.
(31) Wilson, E. B.; Decius, J. L.; Crooss, P. C. *Molecular Vibrations: The Theory of Infrared and Raman Vibrational Spectra*; Dover: New York, 1980.
(32) Colthup, N. B.; Daly, L. H.; Wiberly, S. E. *Introduction to Infrared and Raman Spectroscopy*, 3rd ed.; Academic Press: New York, London, 1990.
(33) Zheng, X.; Zhou, S.; Xiao, Y.; Yu, X.; Feng, B. In Situ Preparation and Characterization of a Novel Gelatin/Poly(D,L-lactide)/Hydroxyapatite Nanocomposite. *J. Biomed. Mater. Res., Part B* **2009**, *91B*, 181−190.
(34) Liu, X.; Zou, Y.; Li, W.; Cao, G.; Chen, W. Kinetics of Thermo-oxidative and Thermal Degradation of Poly(D,L-lactide) (PDLLA) at Processing Temperature. *Polym. Degrad. Stab.* **2006**, *91*, 3259−3265.
(35) Schakenraad, J. M.; Busscher, H. J.; Wildevuur, C. R. H.; Arend, J. Thermodynamic Aspects of Cell Spreading on Solid Substrata. *Cell Biophys.* **1998**, *13*, 75−91.
(36) Allo, B. A.; Costa, D. O.; Dixon, S. J.; Mequanint, K.; Rizkalla, A. S. Bioactive and Biodegradable Nanocomposites and Hybrid Biomaterials for Bone Regeneration. *J. Funct. Biomater.* **2012**, *3*, 432−463.
(37) Armentano, I.; Dottori, M.; Fortunati, E.; Mattioli, S.; Kenny, J. M. Biodegradable Polymer Matrix Nanocomposites for Tissue Engineering: A Review. *Polym. Degrad. Stab.* **2010**, *95*, 2126−2146.
(38) Dadbin, S.; Naimian, F. Gamma Radiation Induced Property Modification of Poly(lactic acid)/Hydroxyapatite Bio-Nanocomposites. *Polym. Int.* **2014**, *63*, 1063−1069.
(39) Di Lorenzo, M. L. Calorimetric Analysis of the Multiple Melting Behavior of Poly(L-lactic acid). *J. Appl. Polym. Sci.* **2006**, *100*, 3145−3151.
(40) Balani, K.; Anderson, R.; Laha, T.; Andara, M.; Tercero, J.; Crumpler, E.; Agarwal, A. Plasma-sprayed Carbon Nanotube Reinforced Hydroxyapatite Coatings and Their Interaction with Human osteoblasts in Vitro. *Biomaterials* **2007**, *28*, 618−624.
(41) Rehman, I.; Bonfield, W. Characterization of Hydroxyapatite and Carbonated Apatite by Photo Acoustic FTIR Apectroscopy. *J. Mater. Sci.: Mater. Med.* **1997**, *8*, 1−8.
(42) Rehman, I.; Smith, R.; Hench, L. L.; Bonfield, W. FT-Raman Spectroscopic Analysis of Natural Bones and Their Comparison with Bioactive Glasses and Hydroxyapatite. *Bioceramics* **1994**, *7*, 79−84.
(43) Mahajan, S. S.; Bambole, M. D.; Gokhale, S. P.; Gaikwad, A. B. Monitoring Structural Defects and Crystallinity of Carbon Nanotubes in Thin Films. *Pramana* **2010**, *74*, 447−455.
(44) Radin, S. R.; Ducheyne, P. The Effect of Calcium Phosphate Ceramic Composition and Structure on in Vitro Behavior. *J. Biomed Mater. Res.* **1993**, *27*, 35−45.
(45) Rey, C.; Combes, C.; Drouet, C.; Lebugle, A.; Sfihi, H.; Barroug, A. Nanocrystalline Apatites in Biological Systems: Characterisation, Structure and Properties. *Materialwiss. Werkstofftech.* **2007**, *38*, 998−1002.
(46) Legeros, R. Z. Calcium Phosphates in Oral Biology and Medicine. *Monogr. Oral Sci.* **1991**, *15*, 1−201.
(47) Kokubo, T.; Takadama, H. How Useful is SBF in Predicting in Vivo Bone Bioactivity? *Biomaterials* **2006**, *27*, 2907−2915.
(48) Zeitlin, B. D.; Joo, E.; Dong, Z.; Warner, K.; Wang, G.; Nikolovska-Coleska, Z.; Wang, S.; Nör, J. E. Antiangiogenic Effect of TW37, a Small-Molecule Inhibitor of Bcl-2. *Cancer Res.* **2006**, *66*, 8698−8706.
(49) Kaneko, T.; Zhang, Z.; Mantellini, M. G.; Karl, E.; Zeitlin, B.; Verhaegen, M.; Soengas, M. S.; Lingen, M.; Strieter, R. M.; Nunez, G.; Nör, J. E. Bcl-2 Orchestrates a Cross-talk between Endothelial and Tumor Cells that Promotes Tumor Growth. *Cancer Res.* **2007**, *67*, 9685−9693.
(50) Pérez, R. A.; Won, J. E.; Knowles, J. C.; Kim, H. W. Naturally and Synthetic Smart Composite Biomaterials for Tissue Regeneration. *Adv. Drug Delivery Rev.* **2013**, *65*, 471−496.
(51) Hasegawa, S.; Neo, M.; Tamura, J.; Fujibayashi, S.; Takemoto, M.; Shikinami, Y.; Okazaki, K.; Nakamura, T. In vivo Evaluation of a Porous Hydroxyapatite/Poly-DL-lactide Composite for Bone Tissue Engineering. *J. Biomed. Mater. Res., Part A* **2007**, *81*, 930−938.
(52) Hasegawa, S.; Tamura, J.; Neo, M.; Goto, K.; Shikinami, Y.; Saito, M.; Kita, M.; Nakamura, T. In Vivo Evaluation of a Porous Hydroxyapatite/ Poly-DL-lactide Composite for Use as a Bone Substitute. *J. Biomed. Mater. Res., Part A* **2005**, *75*, 567−579.
(53) Bi, X.; Patil, C. A.; Lynch, C. C.; Pharr, G. M.; Mahadevan-Jansen, A.; Nyman, J. S. Raman and Mechanical Properties Correlate at Whole Bone- and Tissue-Levels in a Genetic Mouse Model. *J. Biomech.* **2011**, *44*, 297−303.

DOI: 10.1021/acsami.5b01066
ACS Appl. Mater. Interfaces 2015, 7, 9385−9398

(54) Gasior-Glogowska, M.; Komorowska, M.; Hanuza, J.; Ptak, M.; Kobielarz, M. Structural Alteration of Collagen Fibres—Spectroscopic and Mechanical Studies. *Acta Bioeng. Biomech.* **2010**, *12*, 55−62.
(55) Carden, A.; Morris, M. D. Application of Vibrational Spectroscopy to the Study of Mineralized Tissues (Review). *J. Biomed. Opt.* **2000**, *5*, 259−268.
(56) Hofmann, T.; Heyroth, F.; Meinhard, H.; Franzel, W.; Raum, K. Assessment of Composition and Anisotropic Elastic Properties of Secondary Osteon Lamellae. *J. Biomech.* **2006**, *39*, 2282−2294.
(57) Morris, M. D.; Mandair, G. S. Raman Assessment of Bone Quality. *Clin. Orthop. Relat. Res.* **2011**, *469*, 2160−2169.
(58) Morris, D. M. Raman Spectroscopy of Bone and Cartilage. Emerging Raman Applications and Techniques in Biomedical and Pharmaceutical Fields Biological and Medical Physics. *Biomed. Eng.* **2010**, 347−364.
(59) Nyman, J. S.; Makowski, A. J.; Patil, C. A.; Masui, T. P.; O'Quinn, E. C.; Bi, X.; Guelcher, S. A.; Nicollela, D. P.; Mahadevan-Jansen, A. Measuring Differences in Compositional Properties of Bone Tissue by Confocal Raman Spectroscopy. *Calcif. Tissue Int.* **2011**, *89*, 111−122.
(60) Lees, S.; Davidson, C. L.; Rho, J.-Y.; Kuhn-Spearing, L.; Zioupos, P. Mechanical Properties and the Hierarchical Structure of Bone. *J. Biomed. Eng.* **1998**, *20*, 92−102.
(61) Posner, A. S.; Blumenthal, N. C.; Betts, F.; Nriagu, L. O.; Moore, P. B.; Constantz, B. R.; Ison, I. C.; Fulmer, M. T.; Poser, R. D.; Smith, S. T.; Van Wagoner, M.; Ross, J.; Goldstein, S. A.; Jupiter, J. B.; Rosenthal, D. I. Skeletal Repair by in Situ Formation of the Mineral Phase of Bone. *Science* **1995**, *267*, 1796−1799.
(62) Frushour, B. G.; Koening, J. L. Raman Scattering of Collagen, Gelatin, and Elastin. *Biopolymers* **1975**, *14*, 379−391.
(63) Murao, H.; Yamamoto, K.; Matsuda, S.; Akiyama, H. Periosteal Cells are a Major Source of Soft Callus in Bone Fracture. *J. Bone Miner. Metab.* **2013**, *31*, 390−398.
(64) Mikael, P. E.; Amini, A. R.; Basu, J.; Arellano-Jimenez, M. J.; Laurencin, C. T.; Sanders, M. M.; Carter, C. B.; Nukavarapu, S. P. Functionalized Carbon Nanotube Reinforced Scaffolds for Bone Regenerative Engineering: Fabrication, in Vitro and in Vivo Evaluation. *Biomed Mater.* **2014**, *9*, 1−13.
(65) Ren, J.; Zhao, P.; Ren, T.; Gu, S.; Pan, K. Poly(D,L-lactide)/Nano-hydroxyapatite Composite Scaffolds for Bone Tissue Engineering and Biocompatibility Evaluation. *J. Mater. Sci: Mater. Med.* **2008**, *19*, 1075−1082.
(66) Deplaine, H.; Lebourg, M.; Ripalda, P.; Vidaurre, A.; Sanz-Ramos, P.; Mora, G.; Prósper, F.; Ochoa, I.; Doblaré, M.; Gómez Ribelles, J. L.; Izal-Azcárate, I.; Gallego Ferrer, G. Biomimetic Hydroxyapatite Coating on Pore Walls Improves Osteointegration of Poly(L-lactic acid) Scaffolds. *J. Biomed. Mater. Res., Part B* **2013**, *101*, 173−186.
(67) Van der Zande, M.; walboomers, X. F.; Olalde, B.; Alava, J. I.; Boerman, O. C.; Jansen, J. A. Effect of Nanotubes and Apatite on Growth Factor Release from PLLA Scaffolds. *J. Tissue Eng. Regener. Med.* **2011**, *5*, 476−482.
(68) Mahjoubi, H.; Kinsella, J. M.; Murshed, M.; Cerruti, M. Surface Modification of Poly (D,L-Lactid Acid) Scaffolds for Orthopedic Applications: A Biocompatible, Nondestructuve Route via Diazonium Chemistry. *ACS Appl. Mater. Interfaces* **2014**, *6*, 9975−9987.
(69) Heidemann, W.; Jeschkeit, S.; Ruffieux, K.; Fischer, J. H.; Wagner, M.; Krüger, G.; Wintermantel, E.; Gerlach, K. L. Degradation of Poly(D,L)lactide Implants with or without Addition of Calcium Phosphates in Vivo. *Biomaterials* **2001**, *22*, 2371−2378.

NOTE ADDED AFTER ASAP PUBLICATION

This paper was published on the Web on May 4, 2015, with the incorrect artwork for Figure 11. The corrected version was reposted on May 13, 2015.

DOI: 10.1021/acsami.5b01066
ACS Appl. Mater. Interfaces 2015, 7, 9385−9398